Progress in Physics of Applied Materials 6 (2026), Serial Number 127-135

Semnan University

Progress in Physics of Applied Materials

journal homepage: https://ppam.semnan.ac.ir/

Thermal Analysis of Coil-Crucible Configurations in Czochralski Growth of BGO Crystals

Hossein Khodamoradi, Mohammad Hossein Tavakoli*

Physics Department, Bu-Ali Sina University, Hamedan 65174, I.R. Iran

ARTICLE INFO

Article history:
Received: 23 July 2025
Revised: 7 November 2025
Accepted: 17 November 2025
Published online: 3 December 2025

Keywords:
Czochralski method;
Bismuth germanate (BGO);
Induction heating;
Thermal stress;
Finite element simulation;
Crystal-melt interface.

ABSTRACT

This study presents a detailed numerical investigation into the influence of coil-crucible configurations on electromagnetic heating, thermal transport, and stress development during the Czochralski (Cz) growth of bismuth germanate (BGO) crystals. A two-dimensional steady-state finite element model is developed to simulate the coupled behavior of electromagnetic fields, fluid flow, heat conduction, and thermoelastic deformation in both the melt and solid domains. Three distinct coil-crucible arrangements are analyzed to evaluate their effects on the temperature field, melt convection patterns, and the morphology of the crystal-melt interface. The results reveal that strategic modifications in geometry can significantly enhance temperature uniformity while mitigating the magnitude and localization of thermally induced stress within the growing crystal-factors that are critical for reducing defect formation such as dislocations and cracks. Additionally, the study compares two thermal stress estimation approaches, providing a detailed assessment of the resulting stress fields. Validation against available experimental data and literature benchmarks confirms the reliability of the model and underscores the pivotal role of thermal system design in improving crystal quality. These insights provide a practical framework for optimizing coil-crucible configurations to achieve higher-quality oxide crystals in industrial Czochralski growth systems.

1. Introduction

Bismuth germanate (BGO) crystals have been employed across a broad spectrum of applications, ranging from medical devices (such as positron emission tomography) to high-energy physics experiments (including low background spectrometry, high-energy calorimetry, and Compton suppression shield detectors). The optical properties, adequate smoothness of the crystal sides, and the ability to maintain a cylindrical form are crucial features that create BGO crystals suitable for these contexts. The classical high-temperature-gradient Czochralski technique, with its significant advantages, is capable of meeting the requirements to produce these BGO crystals. Furthermore, this method offers cost advantages and enhanced scalability with respect to crystal dimensions, in comparison to the Bridgman and Low Thermal Gradient Czochralski (LTG-Cz) techniques [1]. The growth of Cz-BGO crystals also faces challenges such as a low melt-to-crystal conversion rate, an increased propensity for crystal faceting, and the formation of helical growth patterns [2-4].

Inductive heat generation in the Czochralski (Cz) method often causes uneven heating within the metallic crucible [5–7]. This type of heating not only leads to a convex crystallization front but may lead to solidification of the melt near the crucible bottom as well. Consequently, the melt consumption rate is reduced [1, 8, 9]. Additionally, at the last step of crystal growth, contact between the crystal tip and the crucible bottom increases the possibility of crucible warping. Two main approaches are used to avoid this issue: (1) employing a lower or bottom heater [1, 6, 10],

* Corresponding author.
E-mail address: mht@basu.ac.ir

Cite this article as:

Khodamoradi, H. and Tavakoli, M.H, 2026. Thermal Analysis of Coil-Crucible Configurations in Czochralski Growth of BGO Crystals. *Progress in Physics of Applied Materials*, *6*(2), pp.127-135. DOI: 10.22075/ppam.2025.38367.1157

and (2) modifying the spatial configuration between the coil and the crucible [7, 11-13]. Installing a bottom heater adds energy to the crucible's lower region, raising the local temperature of the melt at the bottom. This effect improves the crucible-coil arrangement, leading to a further optimized thermal gradient within the crucible serving as a passive component.

Currently, numerical modeling serves as a valuable tool for analyzing the process of crystal growth systems in various scenarios. The numerical simulation of BGO crystal pulling has a historic legacy, both in the low-gradient Czochralski (LG-Cz) approach (e.g., [4, 14-18]) and the conventional Cz method [19]. Computational studies of oxide crystal growth, such as BGO, are challenging because of the high Prandtl number characteristic of the melt [20] and the complex temperature distribution within it [21]. Moreover, the semi-transparent nature and other unique optical properties of BGO further complicate these analyses [4, 14, 21].

In this study, three distinct coil-crucible arrangements were examined and their numerical results compared. Changes in inductive heating, fluid flow, temperature distribution, crystal-melt boundary, and thermal stress patterns within the ingot were monitored across various stages of growth while altering the heating system geometry. Subsequently, the effectiveness of each coil-crucible configuration was evaluated under a fixed set of operating conditions, providing a foundational understanding of geometric effects and establishing a baseline for future studies involving parameter optimization.

In this study, three coil-crucible arrangements are investigated: Case 1 - both the crucible and the RF coil exhibit a right cylinder-shaped geometry; Case 2 - a cylindrical crucible coupled with an L-shaped coil; and Case 3 - a crucible featuring a curved bottom corner combined with a coil having a rounded end (Fig. 1).

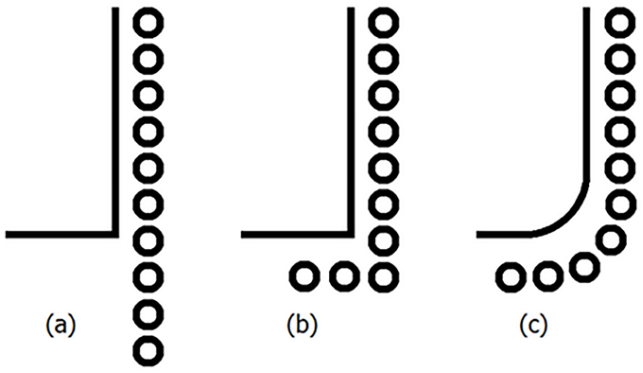

Fig. 1. Schematic of the three coil-crucible geometries studied: (a) Case 1 - simple cylindrical crucible and coil; (b) Case 2 - cylindrical crucible with L-shaped coil; (c) Case 3 - crucible with rounded bottom corner and a coil with a curved terminal segment.

2. Mathematical description

2.1. Inductive heating

The computational model for inductive heating was thoroughly established in the earlier studies, which analyzed the effects of crucible and coil geometries on the heat generation process [7, 22].

2.2. Thermal field

The governing equations for fluid motion, mass conservation, and heat transport were formulated based on the following assumptions: (1) an axially symmetrical configuration under quasi-steady-state conditions; (2) laminar, incompressible, and Newtonian flow behavior for both the melt and the gas, incorporating the Boussinesq approximation; (3) a planar gas-melt interface; and (4) negligible viscous energy loss in both the molten material and the gas. These assumptions were employed to compute the temperature distribution and flow fields [4, 8-9]:

(a)Gas and melt flow

$$\rho\vec{V}.\nabla\vec{V} = -\nabla p + \mu\nabla^2\vec{V} + \rho\beta g(T - T_0)\hat{e}_z \quad (1)$$

(b) Continuity

$$\nabla.\vec{V} = 0 \quad (2)$$

(c) Energy

$$\alpha\nabla^2 T - \vec{V}.\nabla T = 0 \quad (3)$$

(Thermal transport within the fluid domains)

$$k\nabla^2 T + q_{\text{induction}} = 0 \quad (4)$$

(Thermal conduction within the solid domains)

$$k\nabla^2 T = \nabla \cdot \vec{q}_{\text{rad}} = \kappa\left(\int_{4\pi} I(\Omega)d\Omega - 4\pi I_b(T)\right) \quad (5)$$

(Internal radiation in the crystal)

where ρ is the density, $\vec{V}$ is the vector of fluid velocity, p is the pressure, μ is the dynamic viscosity, β is the thermal expansion coefficient, g is the acceleration of gravity, T is the temperature, $\hat{e}_z$ is the unit vector along the pulling axes of z, α is the thermal diffusivity, k is the thermal conductivity, $q_{\text{induction}}$ is the heat source density, κ is the absorption coefficient, and q_{rad} is the radiation heat flux density. In the present estimate, the thermal radiation flux is incorporated into the conduction-driven heat transfer term to account for radiation in the participating medium, specifically the ingot.

The boundary conditions are:

a) No-slip boundary condition at the solid-fluid interfaces

$$\vec{V} = 0 \quad (6)$$

b) Radiative heat exchange at solid-gas boundaries

$$-k_s\frac{\partial T_s}{\partial\hat{n}} = -k_g\frac{\partial T_g}{\partial\hat{n}} + \sum_i F_i\sigma\varepsilon_i(T_s^4 - T_i^4) \quad (7)$$

c) The gas-melt interface is subject to wall-to-wall radiative heat transfer, Marangoni convection, and the no-slip situation.

$$-k_m\frac{\partial T_m}{\partial\hat{n}} = -k_g\frac{\partial T_g}{\partial\hat{n}} + \sum_i F_i\sigma\varepsilon_i(T_m^4 - T_i^4) \quad (8)$$

$$\mu_m\frac{\partial u_m}{\partial\hat{n}} - \mu_g\frac{\partial u_g}{\partial\hat{n}} = \frac{\partial\gamma}{\partial\hat{\tau}} = \frac{\partial\gamma}{\partial T}\frac{\partial T}{\partial\hat{\tau}} \quad (9)$$

(Marangoni effect)

$$V_{\hat{n}} = 0 \quad (10)$$

d) Thermal transport incorporating latent heat generation linked to the growing speed and crystal rotation applied at the crystal-melt boundary.

$$k_m \frac{\partial T_m}{\partial \hat{n}} - k_c \frac{\partial T_c}{\partial \hat{n}} = -\rho_c H_f V_g \quad (11)$$

$$V_\varphi = r\omega_c \quad (12)$$

where the subscripts *s, g, m,* and *c* refer to solid, gas, melt, and crystal, respectively.

e) Radiative heat exchange at the crystal sides based on gray wall theory [14, 23]

$$-k_c \frac{\partial T_c}{\partial \hat{n}} = \varepsilon_c W(T)\left(\sigma T_c^4 - T^{inc}\right) \quad (13)$$

$$V_\varphi = r\omega_c \quad (14)$$

f) Conjugate convective-radiative heat transfer at the external surfaces of the chamber:

$$-k_{\text{ins}} \frac{\partial T_{ins}}{\partial \hat{n}(T_{\text{ins}} - T_{\text{amb}})_{\text{ins}}(T_{\text{ins}}^4 - T_{\text{amb}}^4)} \quad (15)$$

where T_{amb} is the ambient temperature.

2.3. Thermal stress

The stress intensity within crystals can be efficiently prospected by the temperature distribution throughout the solidification procedure, which in turn governs the formation of crystal dislocations [21]. Thermal stress analysis for Czochralski (Cz) growth of oxide crystals has exposed an important increase in thermal stress in semiconductor crystals such as lithium niobate ($LiNbO_3$), which may lead to the formation of cracks during crystal growth and the subsequent cooling process [24-26].

Table 1. Coil-crucible case studies and their respective operating 0

Description (units)	Value
Crucible inner radius (mm)	40
Crucible wall thickness (mm)	2
Crucible inner height (mm)	80
Radius of the round bottom corner of crucible (mm)	12
Coil inner radius (mm)	60
Coil width (mm)	2
Distance between coil turns (mm)	5
Coil turns corner radius (mm)	50

The thermoelastic stress fields in the ingot were computed based on the von Mises stress criterion, using a comprehensive model described in previous work [4]. Furthermore, it has been demonstrated that dislocation density is also associated with the curvature of the temperature distribution [27]. To estimate the dislocation distribution within the crystal, a thermal stress model proposed by Indenbom was employed, represented mathematically as:

$$\sigma = \alpha_T E L^2 \left(\frac{\partial^2 T}{\partial Z^2}\right) \quad (16)$$

where α_T is the thermal expansion coefficient, E is Young's modulus, L is the crystal diameter, and σ is thermal stress.

2.4. Computational parameters

Analysis is conducted on three distinct coil-crucible geometry designs (Fig. 1):

Case 1 - both the crucible and the RF coil have a simple cylindrical shape;

Case 2 - a simple cylindrical crucible combined with an L-shaped coil; and

Case 3 - a crucible with a rounded bottom corner paired with a coil featuring a curved end.

The crystal pulling speed was maintained at 1 mm/h, while the crystal rotation speed was constant at 20 revolutions per minute. Operating parameters of the heating systems are shortened in Table 1. The thermophysical property values used for the calculations are provided in [4].

The BGO melt was considered totally opaque, whereas the BGO crystal was modeled as a semi-transparent region. Additionally, the crystal-melt interface was considered to behave as a black surface. It is worth noting that the gas flow was assumed to be laminar in most growth systems, excluding in the high-pressure Liquid Encapsulated Czochralski (LEC) growth of A3B5 crystals [28].

2.5. Numerical process

In this study, a two-dimensional steady-state finite element method (FEM) was employed to solve the governing equations. The Newton-Raphson iterative algorithm was utilized in conjunction with the direct solver MUMPS (Multifrontal Massively Parallel Sparse Direct Solver [29]). To accurately represent the irregular geometries of the system-including the crystal-melt interface and the curved crucible base in Case 3-unstructured triangular body-fitted elements were used.

A carefully graded mesh distribution was implemented to ensure numerical stability and achieve sufficiently accurate approximations throughout the computational domains. To capture the actual physical behavior, mesh refinement was concentrated near interfaces and regions exhibiting steep gradients in the solution variables.

Table 2. Integrated volumetric heat values in the crucible for each case.

Description (units)	Value
Crucible inner radius (mm)	40
Crucible wall thickness (mm)	2
Crucible inner height (mm)	80
Radius of the round bottom corner of crucible (mm)	12
Coil inner radius (mm)	60
Coil width (mm)	2
Distance between coil turns (mm)	5
Coil turns corner radius (mm)	50

The numerical results were verified by comparison with simulation data reported in Refs. [30, 31]. Additionally, the computational model and material properties were validated against experimental data presented in Ref. [4].

3. Results and Discussion

Fig. 2 depicts the volumetric heat generation profiles, highlighting the differences among the three coil-crucible configurations [7]. A key finding is the systematic attenuation of heating intensity with crystal elongation, despite the persistence of a fixed spatial heat release pattern (governed by the melt height and thermal field; refer to Table 2). This attenuation, evident in all cases, is a direct consequence of the shrinking melt volume, which reduces the thermal energy required to sustain the melting point.

Fig. 3 provides a comparative overview of the thermal and velocity distributions for the three setups. The flow dynamics are marked by a dominant buoyancy-driven vortex in the melt and a dual-vortex structure in the gas phase, which includes a small, intense surface eddy that follows the melt's surface circulation. Crucially, the ensuing temperature gradient is largely defined by the conductive and radiative heat transfer from the crucible surface to the crystal.

A single, large-scale recirculation eddy-driven by buoyancy and observed in systems such as sapphire (Fig. 4) governs the melt flow from the crystal interface downward to the crucible [32]. The influence of this flow pattern is profound, directly controlling the interface morphology and thermal transport. Our analysis found no indication of counter-rotating vortices or substantial turbulence, leading to the conclusion that natural and Marangoni convections are the predominant forces, with forced convection being insignificant.

Resulting from strong buoyancy forces and the poor thermal conductivity of BGO, the temperature distribution displays considerable complexity. Among the configurations, Case 2 stands out for its weaker convection, as manifested by the significantly depressed locations of the maximum temperature, peak velocity, and vortex core. The convective suppression in Case 2 is unambiguously confirmed by its maximum melt velocity of 0.7 cm/s, a value drastically lower than the 1.45 cm/s and 1.51 cm/s measured in Cases 1 and 3.

During the Czochralski growth of BGO, the crystal-melt interface typically assumes a convex morphology, curving toward the melt. This characteristic shape originates from the lower thermal conductivity of the melt compared to the solid phase [21]. The literature frequently attributes this convexity to two primary factors: (1) the prevalence of natural convection within the melt, and (2) radiative heat transfer through the semi-transparent crystal [4, 33].

According to the data in Table 3, the most planar interface morphology is achieved in Case 2, which exhibits the smallest deflection. In contrast, Cases 1 and 3 demonstrate comparable levels of convexity. Simulations extended to longer crystal lengths (5 cm and 15 cm) reveal a progressive deepening of the interface into the melt, with penetrations approximately 20% and 60% greater, respectively, than that observed for the 1 cm crystal (Table 3). This trend is linked to the reduction in melt height during growth, which diminishes the intensity of natural convection and modifies the overall heat transfer dynamics in the melt.

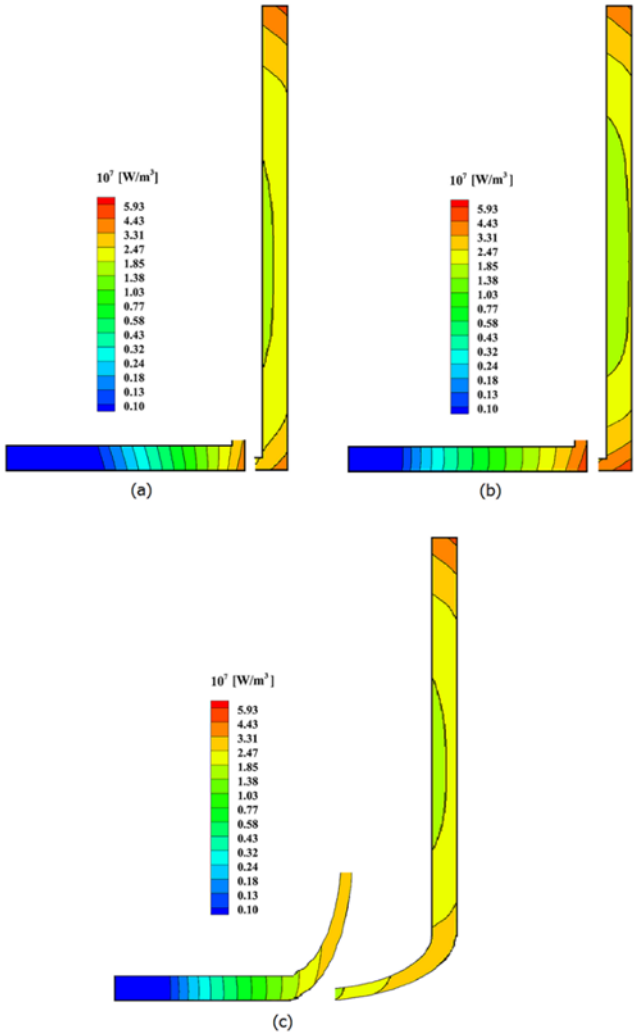

Fig. 2. Distribution of volumetric heat generation in the crucibles for (a) Case 1, (b) Case 2, and (c) Case 3. Enlarged views of the crucible wall and bottom sections are provided for detailed visualization.

Across all growth stages and crystal lengths investigated, Case 2 maintains the most stable solid-liquid interface, demonstrating the smallest height variation. Moreover, the difference in interface deflection between the three configurations becomes more pronounced as the crystal elongates. Specifically, the range between the maximum and minimum curvature height expands from roughly 8% for a 1 cm crystal to nearly 24% for a 15 cm crystal. These significant variations in interface shape are potential contributors to the development of structural defects such as microcracks and faceted interfaces [21].

Simulations of Case 1 at the final growth stage (15 cm crystal) revealed the formation of parasitic crystallization

near the crucible bottom. This observation highlights the critical importance of an optimized heating configuration in suppressing such undesired solidification phenomena and maintaining stable growth conditions.

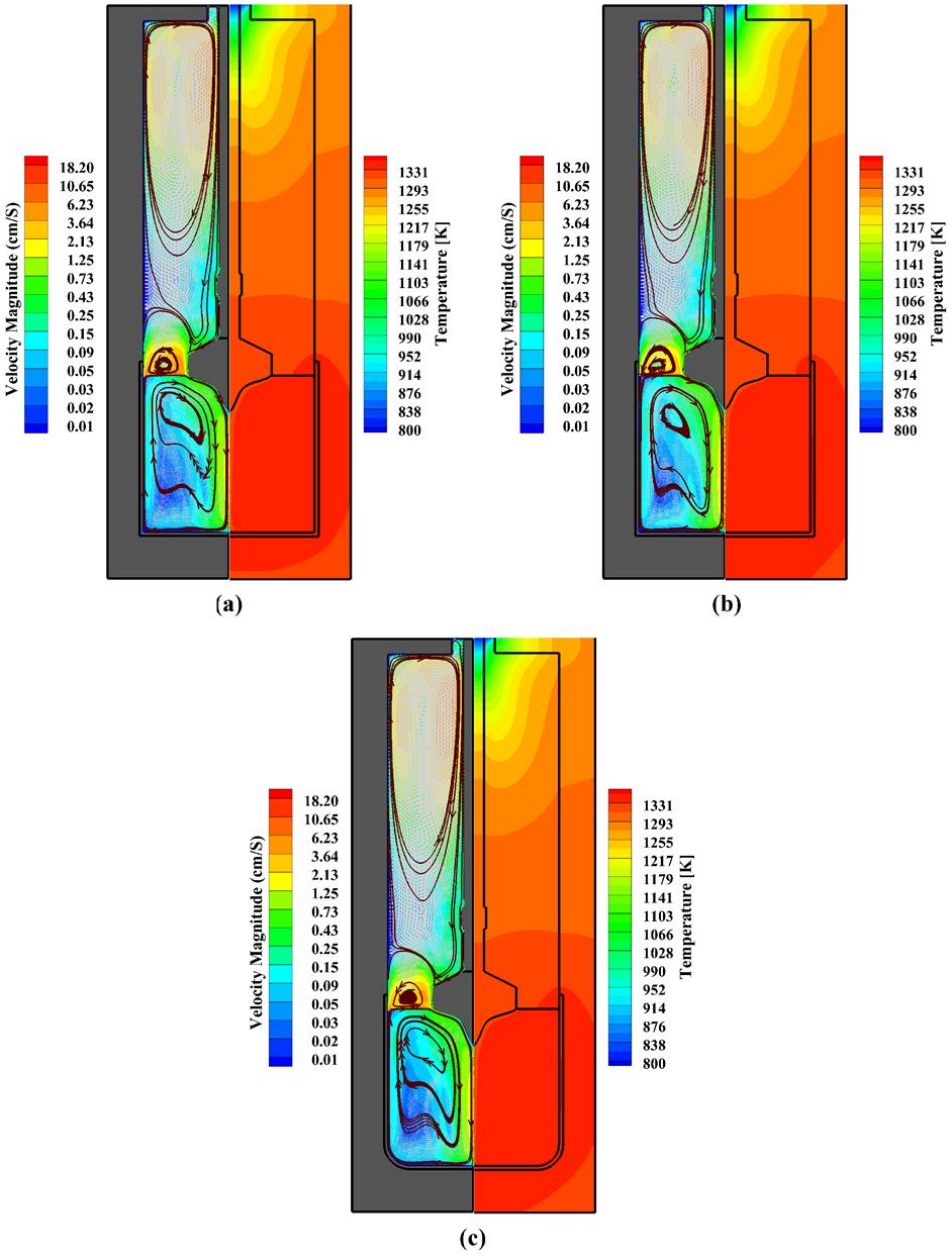

Fig. 3. Temperature (right) and velocity (left) distributions within the entire growth setup for (a) Case 1, (b) Case 2, and (c) Case 3.

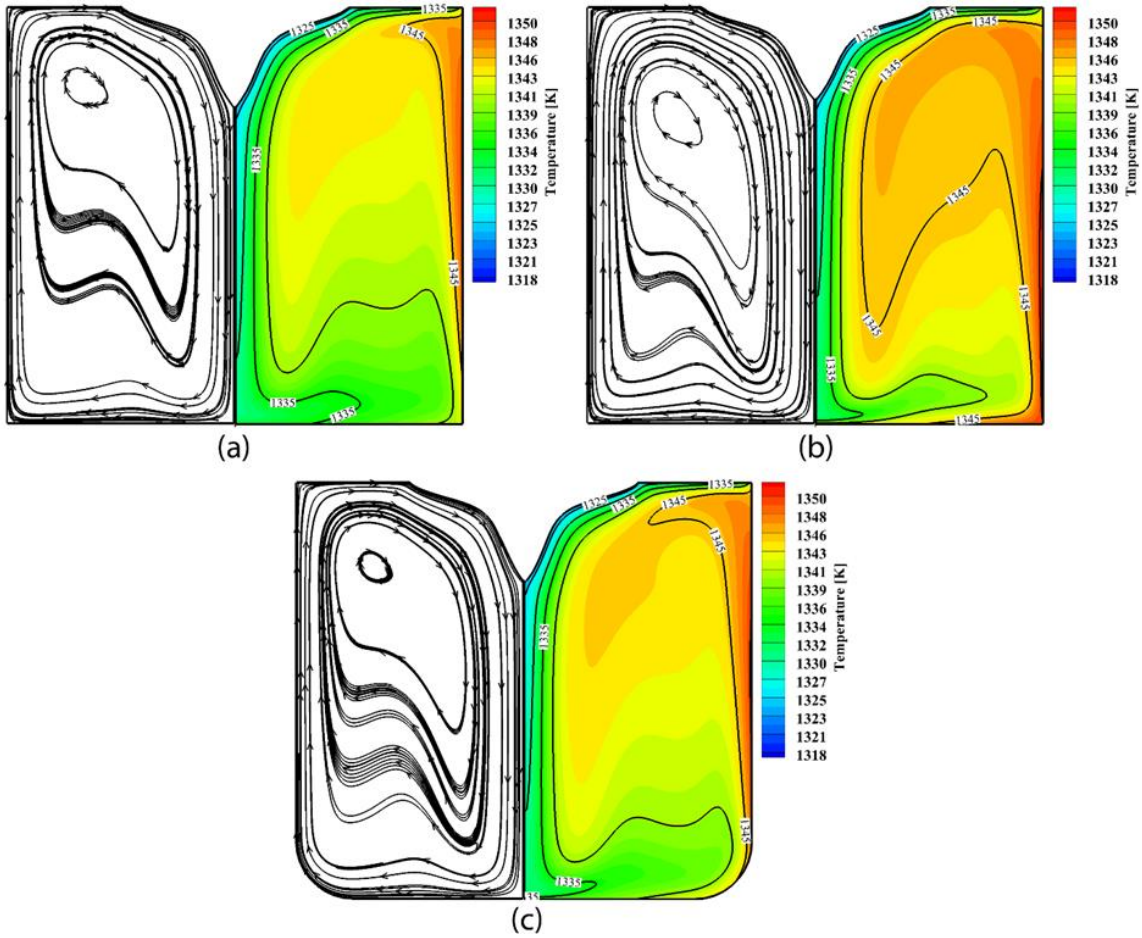

Fig. 4. Visualization of streamlines (left) and temperature distribution (right) in the growth system for (a) Case 1, (b) Case 2, and (c) Case 3.

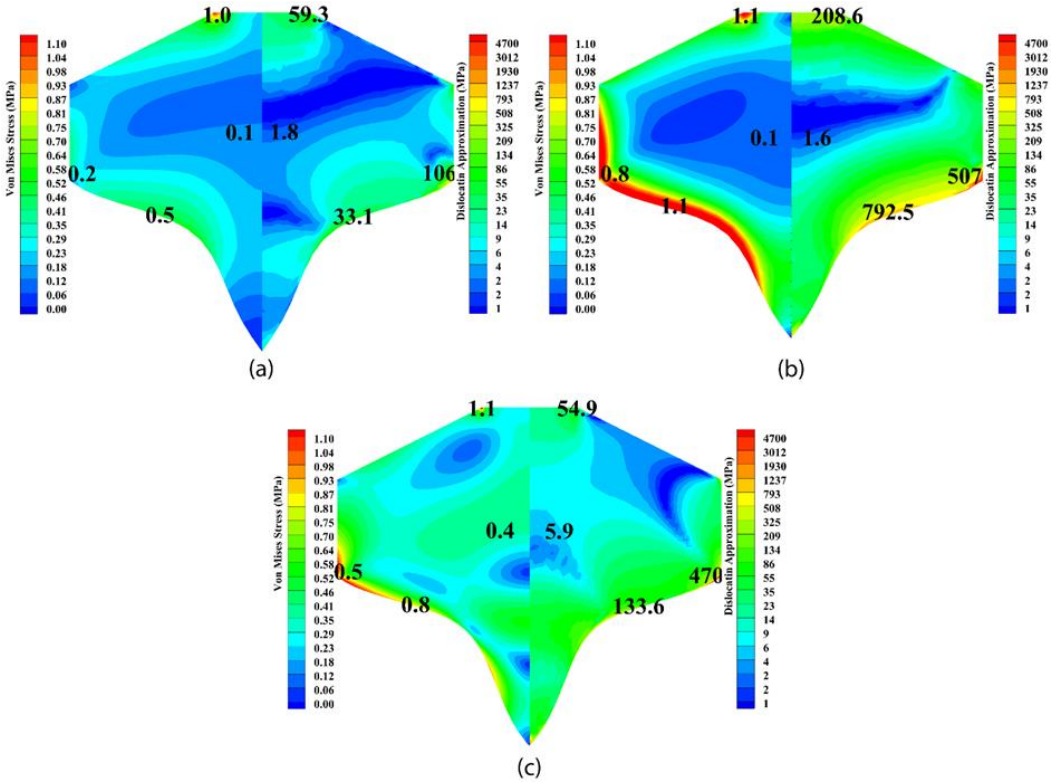

Fig. 5. Von Mises stress distribution as the first-order derivative of thermal stress (left-hand side of each graph) and Indenbom approach as the second-order stress approximation (left-hand side) for (a) Case 1, (b) Case 2 and (c) Case 3.

Table 3. Deflection height at the crystal-melt interface across all cases.

Crystal height (cm)	Case 1 (mm)	Case 2 (mm)	Case 3 (mm)
1	17.6	21.2	28.6
5	16.4	18.9	23.0
15	17.7	21.7	27.2

Fig. 5 offers a comparative analysis of the von Mises stress distribution-a first-order approximation-and the stress field from the second-order Indenbom method for 1 cm long crystals across all cases. A notable discrepancy in stress magnitude is evident between the two techniques. Despite this difference, both models consistently identify the same critical stress concentration zones: the crystal apex, the gas-melt-crystal triple junction (often termed heat accumulation zones), and the crystal-melt interface. Conversely, the crystal center exhibits minimized stress levels in all scenarios.

The von Mises stress analysis identifies the seed region as the location of peak stress intensity across all configurations. Conversely, the second-order Indenbom method delineates a local stress maximum near the seed while locating the global maximum at the triple junction. Of the cases presented in Figure 5, Case 2 yields the most uniform radial stress distribution, extending from the centerline to the crystal periphery. Despite this overall uniformity, both analytical techniques concur that Case 2 is subject to the most pronounced stress accumulation at the crystallization front.

The maximum von Mises stress exhibits a substantial increase throughout the growth process as the crystal elongates, although its value remains similar for different configurations at a given crystal length. At the 1 cm stage, the peak stress lies between 1.0 and 1.2 MPa. By the time the crystal reaches 5 cm, this value rises significantly, with Case 3 recording the highest peak at 5.15 MPa and Case 1 the lowest at 4.21 MPa. In the final stage (15 cm), the thermal stress escalates nearly sixfold, attaining a level of 29-30 MPa universally across all cases.

This level of stress (29-30 MPa) is significant, as published data indicate that the tensile strength of BGO is on the order of ~20-25 MPa **(**e.g., 20.8 MPa measured by Taieb et al., 2025)." [34]. Despite its localization near the seed edge and shoulder, this stress concentration presents a pronounced risk for crack initiation. The formation of a crack at this location could act as a failure origin, enabling propagation along the crown and ultimately degrading the structural integrity and quality of the entire crystal.

The estimation of dislocation density from stress fields requires knowledge of the material's critical shear stress, which is not currently available in the literature for BGO. This fundamental data gap also rendered the implementation of advanced dislocation-based models, including the Alexander-Haasen or Sumino formulations, unattainable for this investigation, necessitating their omission.

The comparative analysis of the von Mises and Indenbom stress criteria reveals not only a quantitative discrepancy but also a fundamental qualitative difference in identifying critical regions. The first-order von Mises criterion effectively highlights areas with high equivalent stress, predominantly near the seed region. In contrast, the second-order Indenbom approximation, being more sensitive to strain gradients, successfully pinpoints the triple junction as the site of the absolute maximum stress - a critical insight for predicting potential crack initiation sites that the von Mises criterion alone could underrepresent. This underscores the value of employing a higher-order stress analysis for a more comprehensive failure risk assessment in crystal growth systems."

While this study provides a detailed analysis of the impact of coil-crucible geometry, it is important to note that the findings are based on a fixed set of process parameters, such as pulling rate, current intensity, and crucible material. A comprehensive investigation into the interaction between these operational parameters and the coil-crucible configuration represents a critical direction for future research. Such a study would further optimize the growth process and enhance the generalizability of the results.

4. Conclusions

A comprehensive set of FE analyses was performed to assess the impact of induction coil and crucible geometry on electromagnetic heating, thermal field characteristics, and stress evolution during the Czochralski growth of BGO single crystals. The simulation outcomes clearly demonstrate that geometric variations in the RF heating system play a significant role in shaping temperature gradients, influencing melt flow dynamics, and determining the morphology of the solid-liquid interface.

The comparative analysis presented in this work underscores the significant influence of coil-crucible geometry on the thermal and stress fields during Czochralski growth of BGO crystals. It is important to note, however, that the conclusions regarding the superiority of a specific configuration, particularly Case 2, are established within the framework of the constant operational parameters adopted in this study, such as the pulling rate, crystal rotation speed, and input current. The interaction between these key process parameters and the geometric design represents a critical area for future investigation. A systematic exploration of parameter space would not only enhance the generalizability of the findings but also pave the way for the development of comprehensive multi-

objective optimization strategies for high-quality crystal growth.

Among the three configurations examined, the L-shaped coil design (Case 2) offered the most thermally stable environment. This setup resulted in weaker melt convection, reduced interface deflection, and a more homogeneous temperature field. These improvements translated into a smoother internal stress distribution and lower peak thermal stress, thereby reducing the likelihood of crack formation and dislocation generation.

The comparison of stress evaluation methods further emphasized the advantage of using second-order thermoelastic formulations for accurately identifying critical stress zones. In later growth stages, the induced thermal stress was found to surpass the tensile strength of BGO in localized regions near the seed and shoulder, highlighting the need for precise thermal management and design optimization.

Overall, the findings underscore the essential role of heating system geometry in enhancing crystal quality and minimizing structural defects. Future Cz system designs should consider the integration of advanced coil geometries, magnetic flux concentrators (MFCs), and refined after-heating techniques. Additionally, extending the present model to three-dimensional domains and coupling it with dislocation-based growth models such as Alexander-Haasen could offer more comprehensive insights into defect evolution mechanisms in oxide crystal growth.

Funding Statement

The authors appreciate the Bu-Ali Sina University for financial support through the Grant number 1002763.

Conflicts of interest

The authors declare that they have no known competing financial interests or personal relationships that could have appeared to influence the work reported in this paper.

Authors contribution statement

Hossein Khodamoradi: Formal analysis, Resources, Methodology, Data curation, Writing Original Draft.

Mohammad Hossein Tavakoli: Methodology, Data curation, Writing - Review & Editing, Supervision.

References

[1] Kolesnikov, A.V., Galenin, E.P., Sidletskiy, O.T. and Kalaev, V.V., 2014. Optimization of heating conditions during Cz BGO crystal growth. *Journal of crystal growth*, *407*, pp.42-47.

[2] Burachas, S.F., Timan, B.L., Kolotii, O.D., Bondar, V.G., Krivoshein, B.I. and Pirogov, E.N., 1997. 5DGLDO LQVWDELOLW\RI ELVPXWK JHUPDQDWH FU\VWDO JURZWK SURFHVV E\&] RFKUDOVNL PHWKRG. *Functional materials*, *2*(4), p.305.

[3] Voszka, R., Gévay, G., Földvári, I. and Keszthelyi-Lándori, S., 1982. Growth and characterization of $Bi_4Ge_3O_{12}$ single crystals. *Acta Physica Academiae Scientiarum Hungaricae*, *53*(1), pp.7-13.

[4] Omid, S. and Tavakoli, M.H., 2018. Effect of the ceramic tube shape on global heat transfer, thermal stress and crystallization front in low thermal gradient (LTG) Czochralski growth of scintillating BGO crystal. *Materials Research Express*, *5*(10), p.105507.

[5] Tavakoli, M.H., Ojaghi, A., Mohammadi-Manesh, E. and Mansour, M., 2009. Influence of coil geometry on the induction heating process in crystal growth systems. *Journal of crystal growth*, *311*(6), pp.1594-1599.

[6] Tavakoli, M.H., Mohammadi-Manesh, E. and Ojaghi, A., 2009. Influence of crucible geometry and position on the induction heating process in crystal growth systems. *Journal of crystal growth*, *311*(17), pp.4281-4288.

[7] Khodamoradi, H., Tavakoli, M.H. and Mohammadi, K., 2015. Influence of crucible and coil geometry on the induction heating process in Czochralski crystal growth system. *Journal of Crystal Growth*, *421*, pp.66-74.

[8] Hadidchi, S. and Tavakoli, M.H., 2023. Influence of Temperature Dependence of Electrical Conductivity of Graphite Crucible in Czochralski Crystal Growth: A Numerical Analysis. *Progress in Physics of Applied Materials*, *3*(2), pp.131-139.

[9] Honarmandnia, M., Tavakoli, M.H. and Sadeghi, H., 2016. Global simulation of an RF Czochralski furnace during different stages of germanium single crystal growth. *CrystEngComm*, *18*(21), pp.3942-3948.

[10] Mazaev, K., Kalaev, V., Galenin, E., Tkachenko, S. and Sidletskiy, O., 2009. Heat transfer and convection in Czochralski growth of large BGO Crystals. *Journal of crystal growth*, *311*(15), pp.3933-3937.

[11] Takagi, K. and Fukazawa, T., 1986. Effect of growth conditions on the shape of $Bi_4Ge_3O_{12}$ single crystals and on melt flow patterns. *Journal of crystal growth*, *76*(2), pp.328-338.

[12] Honarmandnia, M., Tavakoli, M.H. and Sadeghi, H., 2017. Global simulation of an RF Czochralski furnace during different stages of germanium single crystal growth, part II: to investigate the effect of the crucible's relative position against the RF coil on the isotherms, flow fields and thermo-elastic stresses. *CrystEngComm*, *19*(3), pp.576-583.

[13] S. Hadidchi and M. H. Tavakoli, "Impact of Fixed and Moving Crucible on the Ge Crystal Growth Process Numerical Analysis in an Inductively Czochralski Furnace ," *CrystEngComm,* vol. 27, p. 1986–1996, 2025.

[14] Evstratov, I.Y., Rukolaine, S., Yuferev, V.S., Vasiliev, M.G., Fogelson, A.B., Mamedov, V.M., Shlegel, V.N., Vasiliev, Y.V. and Makarov, Y.N., 2002. Global analysis of heat transfer in growing BGO crystals ($Bi_4Ge_3O_{12}$) by low-gradient Czochralski method. *Journal of crystal growth*, *235*(1-4), pp.371-376.

[15] Yuferev, V.S., Budenkova, O.N., Vasiliev, M.G., Rukolaine, S.A., Shlegel, V.N., Vasiliev, Y.V. and Zhmakin, A.I., 2003. Variations of solid–liquid interface in the BGO low thermal gradients Cz growth for diffuse and specular

crystal side surface. *Journal of crystal growth*, *253*(1-4), pp.383-397.

[16] Golyshev, V.D. and Gonik, M.A., 2004. Heat transfer in growing Bi4Ge3O12 crystals under weak convection: II—radiative–conductive heat transfer. *Journal of crystal growth*, *262*(1-4), pp.212-224.

[17] Budenkova, O.N., Vasiliev, M.G., Shlegel, V.N., Ivannikova, N.V., Bragin, R.I. and Kalaev, V.V., 2005. Comparative analysis of the heat transfer processes during growth of $Bi_{12}GeO_{20}$ and $Bi_4Ge_3O_{12}$ crystals by the low-thermal-gradient Czochralski technique. *Crystallography reports*, *50*(Suppl 1), pp.S100-S105.

[18] Vasiliev, M.G., Mamedov, V.M., Rukolaine, S.A. and Yuferev, V.S., 2009. Heat source optimization in a multisection heater for the growth of bismuth germanate crystals by the low-gradient Czochralski method. *Bulletin of the Russian Academy of Sciences: Physics*, *73*(10), pp.1406-1409.

[19] Mamedov, V.M. and Yuferev, V.S., 2009. Time-dependent model of the growth of oxide crystals from melt by the Czochralski method. *Bulletin of the Russian Academy of Sciences: Physics*, *73*(10), pp.1402-1405.

[20] Li, Y.R., Zhang, L., Zhang, L. and Yu, J.J., 2018. Experimental study on Prandtl number dependence of thermocapillary-buoyancy convection in Czochralski configuration with different depths. *International Journal of Thermal Sciences*, *130*, pp.168-182.

[21] B. K. P. V. a. D. M. Dhanaraj G, *Springer Handbook of Crystal Growth*, Berlin: Springer, 2010.

[22] Tavakoli, M.H. and Karbaschi, H., 2021. Numerical study of influences of the input current frequency on the induction heating process. *Progress in Physics of Applied Materials*, *1*(1), pp.44-49.

[23] Guo, Z., Maruyama, S. and Tsukada, T., 1997. Radiative heat transfer in curved specular surfaces in Czochralski crystal growth furnace. *Numerical Heat Transfer, Part A Applications*, *32*(6), pp.595-611.

[24] Tsukada, T., Kakinoki, K., Hozawa, M., Imaishi, N., Shimamura, K. and Fukuda, T., 1997. Numerical and experimental studies on crack formation in $LiNbO_3$ single crystal. *Journal of Crystal Growth*, *180*(3-4), pp.543-550.

[25] Miyazaki, N., Uchida, H., Tsukada, T. and Fukuda, T., 1996. Quantitative assessment for cracking in oxide bulk single crystals during Czochralski growth: development of a computer program for thermal stress analysis. *Journal of crystal growth*, *162*(1-2), pp.83-88.

[26] Kobayashi, M., Tsukada, T. and Hozawa, M., 2002. Effect of internal radiation on thermal stress fields in CZ oxide crystals. *Journal of crystal growth*, *241*(1-2), pp.241-248.

[27] Indenbom, V.L., 1979. Ein Beitrag zur Entstehung von Spannungen und Versetzungen beim Kristallwachstum. *Crystal Research and Technology*, *14*(5), pp.493-507.

[28] Ofengeim, D.K. and Zhmakin, A.I., 2003, June. Industrial challenges for numerical simulation of crystal growth. In *International Conference on Computational Science* (pp. 3-12). Berlin, Heidelberg: Springer Berlin Heidelberg.

[29] Available: http://mumps.enseeiht.fr/.

[30] Kobayashi, N., 1981. Hydrodynamics in Czochralski growth-computer analysis and experiments. *Journal of Crystal Growth*, *52*, pp.425-434.

[31] Tavakoli, M.H., Omid, S. and Mohammadi-Manesh, E., 2011. Influence of active afterheater on the fluid dynamics and heat transfer during Czochralski growth of oxide single crystals. *CrystEngComm*, *13*(16), pp.5088-5093.

[32] Stelian, C., Sen, G. and Duffar, T., 2018. Comparison of thermal stress computations in Czochralski and Kyropoulos growth of sapphire crystals. *Journal of Crystal Growth*, *499*, pp.77-84.

[33] Banerjee, J. and Muralidhar, K., 2006. Role of internal radiation during Czochralski growth of YAG and Nd: YAG crystals. *International journal of thermal sciences*, *45*(2), pp.151-167.

[34] Taieb, K., Belkhir, N., Khennab, A., Rogers, E., Giusca, C. and Bizarri, G., 2025. High-precision machining behavior of the single crystal scintillator, bismuth germanate ($Bi_4Ge_5O_{12}$). *Materials Today Communications*, p.112620.